Supplementary Material for: Low-Amplitude Action Potential Voltage Alternans Precedes Arrhythmogenic Spatially Discordant Alternans in Human Heart Failure

1 Manuscript and Supplement Abbreviations

Table 1 Abbreviations

Acronym	Definition
APD	Action Potential Duration
APV-ALT	Action Potential Voltage Alternans
AT	Activation Time
C_{alt}	Calcium Transient Alternation
CaT-ALT	Calcium Transient Alternans
CL	Cycle Length
HF	Heart Failure
HVM	Human Ventricles Models
k-score	dimensionless alternans magnitude above noise
LV	Left Ventricle
LVEF	Left Ventricular Ejection Fraction
MAP	Monophasic Action Potential
SR	Sarcoplasmic Reticulum
Rdiff	Repolarization Map difference
Rmap	Repolarization Map
RT	Repolarization Time
RT-ALT	Repolarization Time Alternans
RV	Right Ventricle
SD	Standard Deviation
V_{alt}	Voltage Alternation
VF	Ventricular Fibrillation
Vm	Transmembrane Voltage
VT	Ventricular Tachycardia

Table 1: List of all abbreviations used throughout the manuscript and this supplement.

2 Image-based Geometry and Fiber Orientation

The human ventricles model used for this study has been published in [1], please refer to Figure S10 of its supplement. In brief, the geometry and fiber orientation of an adult human heart were imaged at Johns Hopkins University [2], then constructed into a mathematical model using the methodology of Vadakkumpadan et al [3]. The human ventricular geometry was segmented from magnetic resonance images using the level set method, then meshed with the software package Tarantula [4] to yield a 2,423,911 node and 2,929,297 element mesh with an average element edge length of 475μm. The fiber orientation, i.e. the macroscopic representation of myocyte organization throughout the myocardium, was assigned to the finite elements of the mesh using tensors derived from diffusion tensor images.

3 Membrane Kinetics and Simulation Software

For the large-scale simulation studies in the human ventricles model, the dynamical pacing protocol requires solving several minutes of simulation time on ventricular meshes containing millions of nodes, which is computationally demanding. For this reason, we to chose to represent the membrane kinetics in the human ventricles model with the ten Tusscher-Panfilov (TTP) human ventricular myocyte model [5, 6]. This particular model was chosen since it is proven to produce physiological electrical alternans [6], and to be computationally efficient with a minimal number of state variables to compute on each node of the human ventricles mesh [35]. To account for spatial heterogeneity in both non-failing and failing electrophysiology, the TTP myocyte model was modified according to sections 5 and 6.

Monodomain simulations were performed with the human ventricles model using the Cardiac Arrhythmia Research Package [7] (CARP by CardioSolv LCC) running on 16

compute nodes, each with four Dual Core AMD Opteron processors (Model 2222) and 8GB of memory. All simulations conducted in CARP with this modeling setup used a 20 μs time step.

4 Model Parameterization for Applying Heterogeneities

Apicobasal and transmural heterogeneities in conduction [8], calcium handing [9], and action potential dynamics [10, 11] exist in the human heart. In order to apply apicobasal and transmural heterogeneities to the human ventricles model, the apicobasal and transmural directions in the mesh were parameterized using Function 1 of the Laplace-Dirichlet method outlined in Bayer et al [12]. Figure 1A shows the results for the parameterization of the apicobasal direction (Φ_{ab}), where the scalar field took on its maximum in the apex and its minimum at the base of the ventricles. Figure 1B shows the results for the parameterization of the transmural direction (Φ_{tran}), where the scalar field took on its maximum on the epicardial surface, and its minimum on the endocardial surface. Please note, Φ_{tran} was the combination of the Φ_{epi} and Φ_{lv} fields in Bayer et al [12] to make the septum an extension of the LV free wall. This is consistent with the study by Keller et al [13] to produce an action potential duration (APD) gradient naturally found across mammalian ventricular septum [14].

Once Φ_{ab} and Φ_{tran} were computed, for any node or element in the human ventricles mesh (n), ion channel conductances and tissue conductivities (X_i) could then be interpolated throughout the myocardium along both the apicobasal and transmural axes using the equation,

$$X_i(n) = \Phi_{ab}(n) * \Phi_{tran}(n) * (\Omega_{epi} - \Omega_{endo}) + \Omega_{endo} \quad (1)$$

Ω_{epi} and Ω_{endo} were constants on the epicardial and endocardial surfaces of the human

ventricles model, and were chosen based on experimental data (see section 5). If either apicobasal or transmural heterogeneity was not desired for a given model parameter (X_i), then the corresponding Φ was set to 1.0 for all n. Also note, for all X_i in the human ventricles model, maximum Φ_{tran} = 1 and minimum Φ_{tran} = 0, where only $X_{I_{Ks}}$ had bounds for Φ_{ab} not equal to 0.0 or 1.0 (see section 6). The values obtained with equation 1 were then used as inputs to the CARP simulator in order to modify the TTP model on a per mesh node basis, and the tissue conductivities on a per mesh element basis.

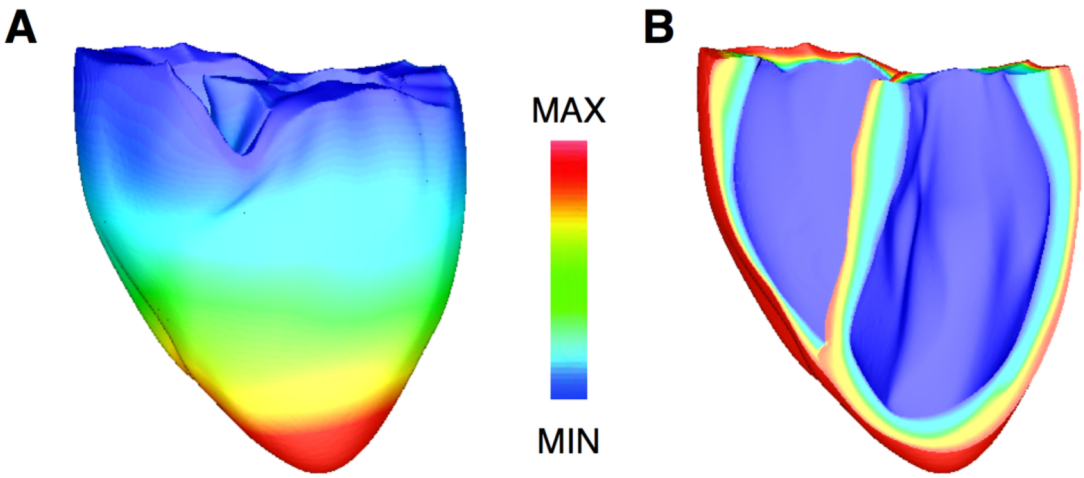

Figure 1: (A) Apicobasal parameterization Φ_{ab}. (B) Transmural parameterization Φ_{tran}.

5 Transmural Heterogeneity

Transmural heterogeneities in tissue conductivity and ion channel conductance were included into the human ventricles model to corroborate simulation results with the most recent optical mapping studies on healthy and failing myocardium [8–10]. The myocardial tissue conductivities were adjusted to match experimentally measured conduction velocities (CV) [8], then the ionic model parameters in the TTP model were spatially adjusted along the transmural axis of the ventricular walls to match transmural calcium

transient duration (CaTD) [9] and APD [10] observed in normal and failing human myocardium. Modeling these heterogeneities is essential since CV, calcium handling, and action potential dynamics can all affect the magnitude and rate-dependence of the cardiac alternans investigated in the manuscript.

5.1 Dynamic Pacing Protocol for Parameter Adjustments

To adjust tissue conductivity and TTP parameters in models of healthy and failing human myocardium, the same dynamic pacing protocol for the optical mapping studies [8–10] was used. The endocardium was paced for 1 minute at sequential pacing cycle lengths (CL in ms) of 4000, 2000, 1500, 1000, 900, 800, 750, 700, 650, 600, 550, 500, 450, 420, 400, 380, 360, 350, 340, 330, 320, and then in steps of 10 ms until 1:1 capture failed.

Ionic model parameters were adjusted until they simultaneously satisfied the following three criteria: 1.) ionic channel conductance changes were within physiological ranges, as reported in the literature; 2.) the measurement of interest (APD, CaT duration, etc.) was within the standard deviation of the experimental or clinical data; and 3.) alternans developed at pacing CLs $\leq$ 550 ms.

5.2 Transmural Left Ventricular Tissue Model

Due to the long simulation times (months) and large amounts of data storage (petabytes) required to perform the dynamic pacing protocol (section 5.1) in the entire human ventricles model, iteratively adjusting the tissue conductivities and TTP parameters to match experimental data was performed more efficiently using a small transmural LV tissue model taken from the same location as in the optical mapping studies [8–10]. This simplification is possible since these optical mapping studies predominately analyzed transmural wavefront propagation from the endocardium to the epicardium in isolated LV tissue preparations

The LV tissue model used to determine the transmurally heterogeneous model parameters for tissue conductivity and ion channel conductances had the dimensions 1.8cm (transmural) $\times$ 0.95cm (apicobasal) $\times$ 0.95cm (circumferential), which closely matched the transmural dimension of the tissue preparations described in Figure 1 of Glukhov et al [10]. The LV tissue model was discretized to have an average element edge length of 475μm, which matched the average element edge length of the mesh. By matching the average element edge lengths, CV was equivalent in the two models when using the same set of tissue conductivities [15]. The effect of tissue anisotropy on CV was also included into the transmural LV tissue model by using the rule-based fiber generation algorithm in Bayer et al [12]. The α (fiber angle) and β (sheet angle) parameters in the algorithm were adjusted to match the image-based transmural fiber and sheet angles in the human ventricles model (α_{endo} = 50°, α_{epi} = -75°,β_{endo} = -50° β_{epi} = 40°).

5.3 CV Heterogeneity

Using the transmural LV tissue model, tissue conductivities were systematically adjusted according to [16] in the endocardium and epicardium to match CVs measured experimentally in both nonfailing and failing human myocardium [8]. Table 2 displays the results for the conductivities determined to produce the baseline CVs measured in Glukhov et al [8] for both normal and failing myocardium listed in Table 3. CVs in the model were computed using the same approach as Glukhov et al [8]. Furthermore, only the conductivity σ_t was interpolated from endocardium to epicardium since CV_l and CV_n were only measured experimentally on the epicardial surface of the LV tissue preparations. Measuring CV with optical mapping on the endocardium is very difficult due to the presence of papillary muscles and trabecula. Also note, since evidence for apicobasal CV heterogeneity in the human ventricles was not found in the literature, Φ_{ab} was held constant at 1. Figure 2 shows the results for rate-dependent transmural CV in the LV tissue model,

using the values in Table 2 with equation 1, in comparison to the CV data measured by Glukhov et al [8].

Table 2 Model Conductivities

	Ω_{endo}	Ω_{epi}
Normal Tissue:		
σ_l (S/m)	0.280	0.280
σ_t (S/m)	0.085	0.065
σ_n (S/m)	0.032	0.032
Failing Tissue:		
σ_l (S/m)	0.280	0.280
σ_t (S/m)	0.045	0.025
σ_n (S/m)	0.021	0.021

Table 2: Orthotropic intracellular tissue conductivities along the fiber (σ_l), transverse the fiber (σ_t) and in the direction of the sheet normal (σ_n) assigned to the ventricular models to match the CVs in Table 3.

Table 3 Experimental CVs

	Endocardium	Epicardium
Normal Tissue:		
CV_l (cm/s)	-	92±4
CV_n (cm/s)	-	22±2
CV_{tran} (cm/s)	47±5	38±5
Failing Tissue:		
CV_l (cm/s)	-	91±6
CV_n (cm/s)	-	16±2
CV_{tran} (cm/s)	33±5	24±5

Table 3: CVs measured experimentally by Glukhov et al [8] with the pacing CL of 1000 ms. CV along fibers (CV_l) and sheet normals (CV_n) were obtained by optically mapping the LV epicardial surface. Transmural CV (CV_{tran}) was obtained by optically mapping transmural conduction in the LV wall. Regions where CV was not able to be measured experimentally are marked with -.

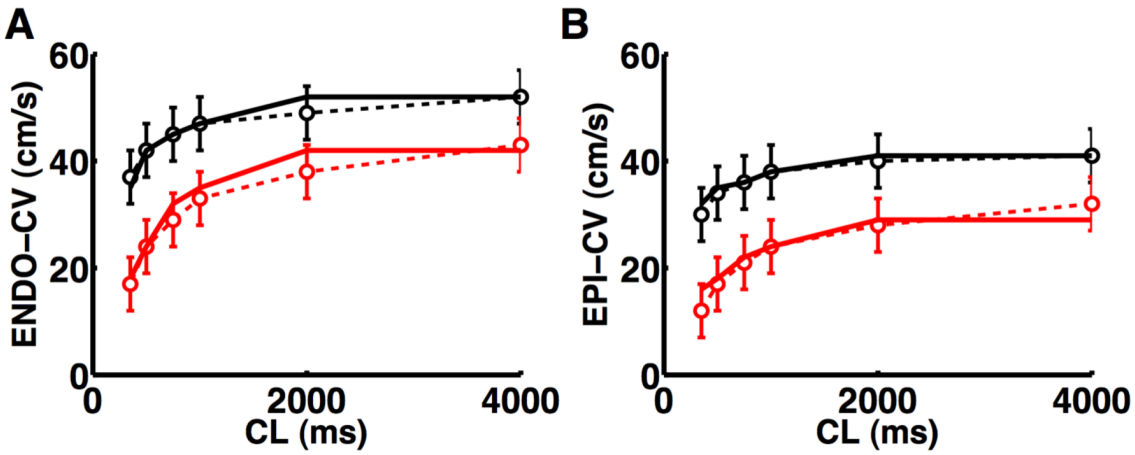

Figure 2: CV restitution curves for the subendocardium (A) and subepicardium (B) of the nonfailing (black) and failing left ventricle (red). The experimental data from Glukhov et al [8] are plotted as dashed lines and the modeling data from the transmural LV tissue model are plotted as solid lines.

5.4 CaTD Heterogeneity

The CaTD produced with the default TTP model was more than 100 ms shorter than that observed in the optical mapping study by Lou et al [9]. Thus, to preserve the peak calcium transient in the model, but prolong its duration, the maximal conductance for sarcoplasmic reticulum calcium uptake (I_{up}) and leak (I_{leak}) were decreased, while the inactivation time constant for the L-type calcium current (τ_f) was increased. These three changes were made simultaneously in both the endocardium and epicardium until CaTD was within the data ranges of the experimental data in Figure 4 of Lou et al [9]. The values determined for the TTP model to be used in equation 1 to match the control data in Figure 3 can be found in Table 4.

Table 4 Control Calcium Model Parameters

	Ω_{endo}	Ω_{epi}
V_{maxup} (mM/ms)	0.003825	0.004399
V_{leak} (mM/ms)	0.000216	0.000248
τ_f	x1.4	x1.3

Table 4: Parameters of the TTP model [6] that were adjusted in the endocardium and epicardium to be applied to equation 1 to match the control data in Lou et al [9].

Both SERCA2a mRNA/protein levels [17, 18] and function (Iup) [19, 20] have been shown to be decreased in heart failure (HF), in addition to a transmurally heterogeneous downregulation of SERCA2a (Figure 8 of Lou et al [9]). Thus, the maximal Iup conductance (V_{maxup}) was reduced by 50% on the endocardium, and only by 30% on the epicardium. An increase of sodium-calcium exchange mRNA/protein levels [17] and function (I_{NaCa}) [21] have also been reported in human HF studies. Thus, maximal I_{NaCa} (k_{NaCa}) was increased by 55% for both the endocardium and epicardium. Lastly, calcium

leakage from the sarcoplasmic reticulum is increased in HF [22, 23] and promotes alternans [24]. Thus, as done in previous HF studies [25, 26], the maximal leak conductance (V_{leak}) was more than doubled (x2.25). Figure 3 shows the results for rate-dependent transmural CaTD in the failing LV tissue model, using the values in Table 5 with equation 1, in comparison to the HF CaTD data measured by Lou et al [9].

Table 5 Heart Failure Calcium Model Parameters

	Ω_{endo}	Ω_{epi}
V_{maxup} (mM/ms)	0.001913	0.002859
k_{NaCa} (pA/pF)	1550	1550
V_{leak} (mM/ms)	0.000488	0.000561

Table 5: Parameters of the TTP model [6] that were adjusted in the endocardium and epicardium to be applied to equation 1 to match the HF data in Lou et al [9].

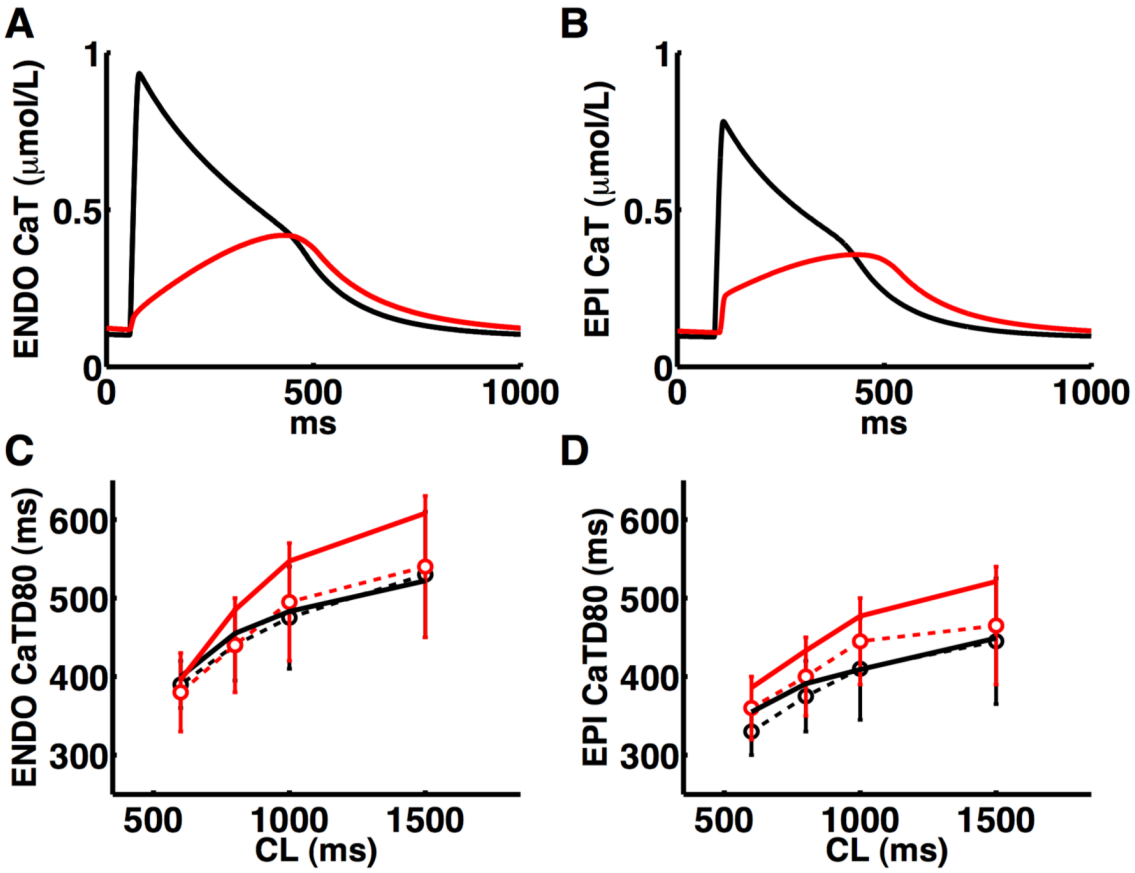

Figure 3: Calcium transients plotted at CL = 1500 ms for the endocardium (A) and epicardium (B) of the nonfailing (black) and failing (red) left ventricle. Rate-dependent CaTD at 80% recovery for the subendocardium (C) and subepicardium (D) from experimental data [9] (dashed lines) and from the transmural LV tissue model (solid lines).

5.5 APD Heterogeneity

In healthy myocardium, there is a transmural gradient of APD across the ventricular walls, with the longest APD on the endocardium and the shortest APD on the epicardium [10]. This APD gradient has been shown to be essential for simulating cardiac electrophysiology consistent with patient data [13]. Thus, a linear APD gradient across the ventricular walls was included into the human ventricles model according to Glukhov et al [10]. To match the endocardial and epicardial APDs measured experimentally, the maximal conductance of I_{Ks}, which is heterogeneous across the human ventricular wall [27], was set

to 0.159 nS/pF on the endocardium and 0.392 nS/pF on the epicardium. Using these values as the Ω in equation 1, the transmural APDs produced in the LV tissue model compared well to the experimental data (Figure 4) from Glukhov et al [10] at pacing CL used for the studies in the manuscript ($\leq$ 1000 ms).

In human HF, APD is significantly prolonged and has been attributed to reductions in I_{K1} [28], I_{Ks} [29], I_{to} [30], and increased I_{NaL} [31]. Accordingly, in the failing human ventricles model, maximal conductance was reduced for I_{K1} by 25%, I_{Ks} by 50%, and I_{to} by 35%. To include the contributions from increased I_{NaL}, the formulation of the late sodium current in O'Hara et al [32] was added to the TTP model, then its maximum conductance increased by 12 fold [31]. Contributions from I_{NaL} in the control TTP model, and its tranmsural heterogeneity [32], had little effect on APD dynamics.

Lastly, Glukhov et al [10] showed that prolongation of APD in human HF is not homogeneous across the ventricular walls, occurring predominately in the endocardium of failing human myocardium. The end result is a loss of the transmural APD gradient as shown in Glukhov et al [10]. To approximate the loss of transmural APD gradient, the maximal conductance for I_{Ks} was held constant across the ventricular walls. The results of applying these modifications to the TTP model (Table 6), and then to the failing LV tissue model using equation 1, can be found in Figure 4.

Table 6 Heart Failure Action Potential Model Parameters

	Ω_{endo}	Ω_{epi}
G_{K1} (nS/pF)	4.054	4.054
G_{Ks} (nS/pF)	0.196	0.196
G_{to} (nS/pF)	0.0475	0.191
G_{NaL} (mS/μF)	0.09	0.054

Table 6: Parameters of the TTP model [6] that were adjusted in the endocardium and epicardium to be applied to equation 1 to match the HF data in Glukhov et al [10].

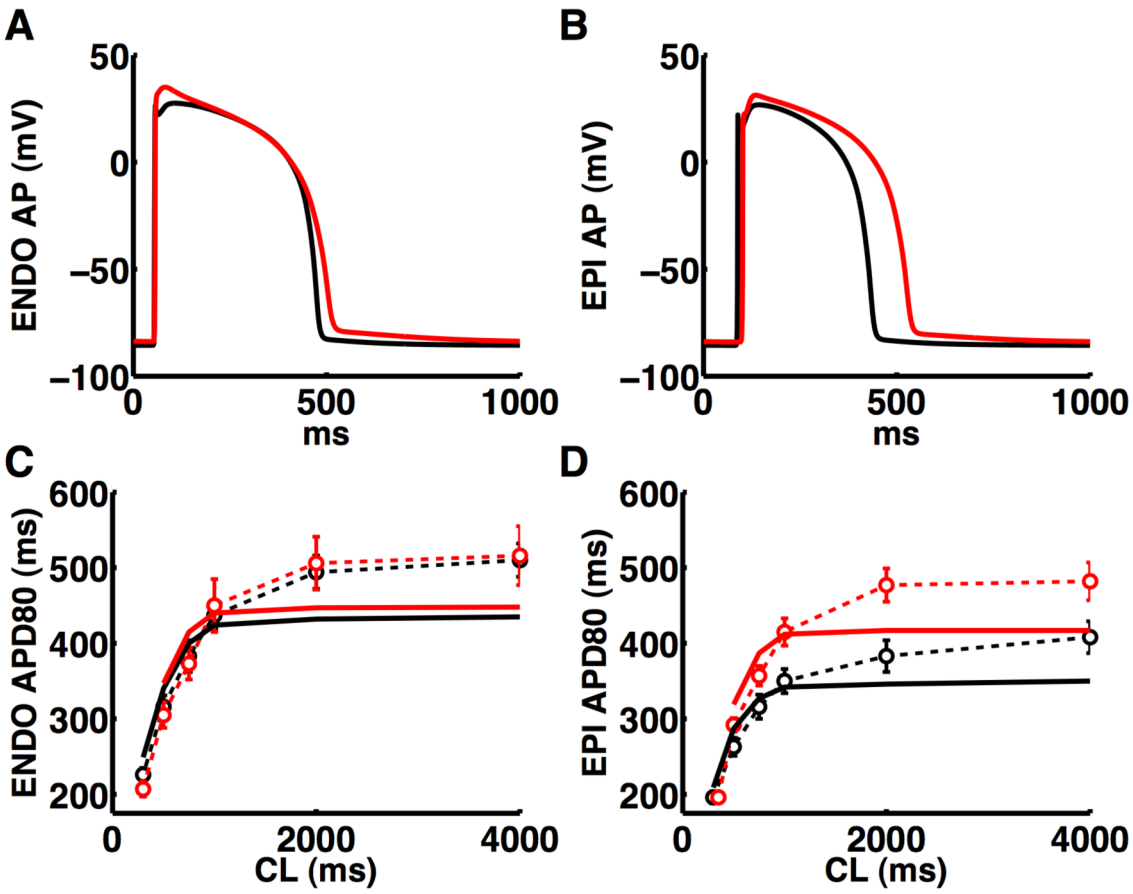

Figure 4: Action potentials plotted at CL = 1000 ms for the endocardium (A) and epicardium (B) of the nonfailing (black) and failing (red) left ventricle. Rate-dependent APD at 80% repolarization for the subendocardium (C) and subepicardium (D) from experimental data [10] (dashed lines) and from the transmural LV model (solid lines).

6 Apicobasal Heterogeneity

APD is shorter in the apex than in the base, which can be explained by a heterogeneous apicobasal distribution of I_{Ks} channels [11]. Including apicobasal heterogeneity in computer models of the heart is essential to reproduce ECGs of patients [13, 33, 34]. Apicobasal heterogeneity of the maximal conductance of I_{Ks} ($X_{G_{Ks}}$) was interpolated into the human ventricles model using equation 1 with the minimum $\Phi_{ab} = 0.616$, so that G_{Ks} was equal to the smallest G_{Ks} in the default TTP model (0.098 nS/pF) [6], $\Phi_{ab} = 1.0$ midway between the apex and base, so that APD in this region directly corresponded to

the location APD was measured in the optical mapping studies [8–10], and the maximum Φ_{ab} = 5.0 in the apex, so that APD in the apex of the model matched the patient data in Table 2 of Narayan et al [35]. As mentioned previously, for all other model parameters, Φ_{ab} is fixed to 1.0 for every mesh node and element of the model.

7 Comparisons with local clinical signals and complex APD oscillations

Local clinical signals were recorded as monophasic action potentials (MAPs), so APV-ALT frequency spectra and complex APD oscillations (described below) at specific locations in the HVM were computed from simulated MAPs to compare with their respective results in clinical MAPs, which are spatially averaged approximations of the transmembrane voltage underlying the tip of the recording MAP electrode ($\sim$0.25cm^2). APV-ALT does not contain phase information for transmembrane voltage, but its spectrum can broaden across lower frequencies due to spatially discordant oscillations in transmembrane voltage around the MAP catheter tip. Furthermore, spatial averaging of local MAP signals can alter the phase of local AT and APD measurements. Thus, APV-ALT frequency spectra and complex APD oscillations (described below) at specific locations in the HVM were computed from simulated MAPs to compare with their respective results in clinical MAPs.

MAPs were computed by first choosing HVM surface nodes in regions of concordant and discordant RT-ALT. Then for each HVM surface node, all HVM mesh nodes within a 1.15mm radius ($\sim$7F catheter radius) were assigned a fixed transmembrane voltage of -40.0mV with membrane resistance of 1 kΩ·cm^2. MAPs were computed by differencing the extracellular potentials between the MAP surface nodes and a reference node 1cm above the surface [36]. Extracellular potentials were computed according to Gima et al [37]. APV-ALT and APD were computed in the simulated MAPs the same way as in

patients [35].

Spatially discordant electrical alternans may manifest as complex APD oscillations in MAPs, as shown in the human atria [38]. Complex APD oscillations [39, 40], i.e. variations $>2.5\%$ in APD (above noise and sampling artifacts in MAPs) but not alternating in phase from beat to beat for >5 beats, have been observed in HF patients that exhibited APV-ALT and experienced VT/VF during long-term follow-up [35]. Using this same criteria, we analyzed the simulated MAPs in the failing HVM for the last 8 beats at each pacing CL of the alternans pacing protocol for complex APD oscillations in regions of concordant and discordant RT-ALT. These results were used to determine if complex APD oscillations alter the spectrum of APV-ALT and are linked to spatially discordant RT-ALT.

8 Supplemental Clinical Data: Patient Follow-up

Table 7 Demographics of Clinical Cohort

	LV Dysfunction (n=53)	Preserved LV (n=18)	
Age, y	65.4±13.3	65.8±10.6	0.91
Gender, M/F	52/1	15/3	<**0.05**
Ejection fraction, %	28±8	58±12	<**0.001**
Coronary disease, n	47	4	<**0.001**
Hypertension, n	11	3	0.71
Diabetes Mellitus, n	8	2	0.67
BNP, pg/ml	640±825	131±282	<**0.05**
Medication use, %			
Beta blockers	39	7	<**0.01**
ACE inhibitors/ARB	47	11	<**0.01**
Spironolactone	10	1	0.18
CCB	11	4	0.89
Digoxin	21	2	<**0.05**
Amiodarone	5	1	0.61
Statins	38	9	0.09

Table 7: Demographics for all patients in the supplement and manuscript.

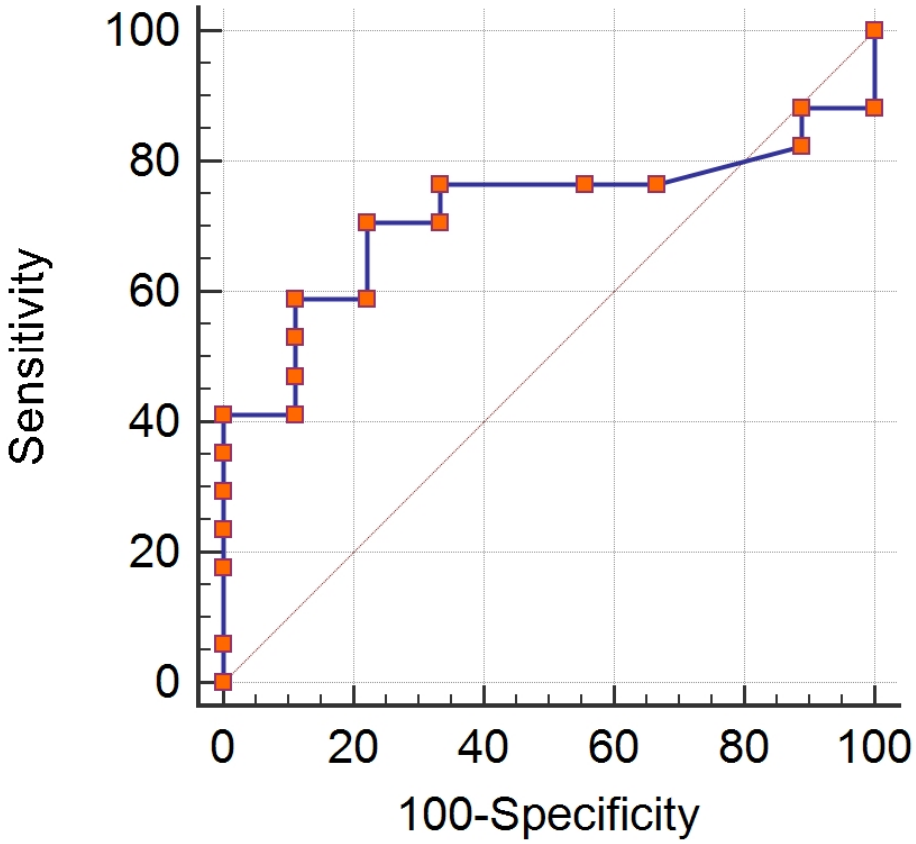

Figure 5: Receiver operating characteristics for determining the optimal cutpoint of ΔAPD to predict long-term ventricular arrhythmias in study patients. The ROC curve for positive (n=17) and negative (n=9) patient groups has an area under the curve of 0.72±0.10, a Youden index J=0.4837 with associated criterion ≥2.3% of mean APD, and a 70.59% sensitivity with a 77.78% specificity.

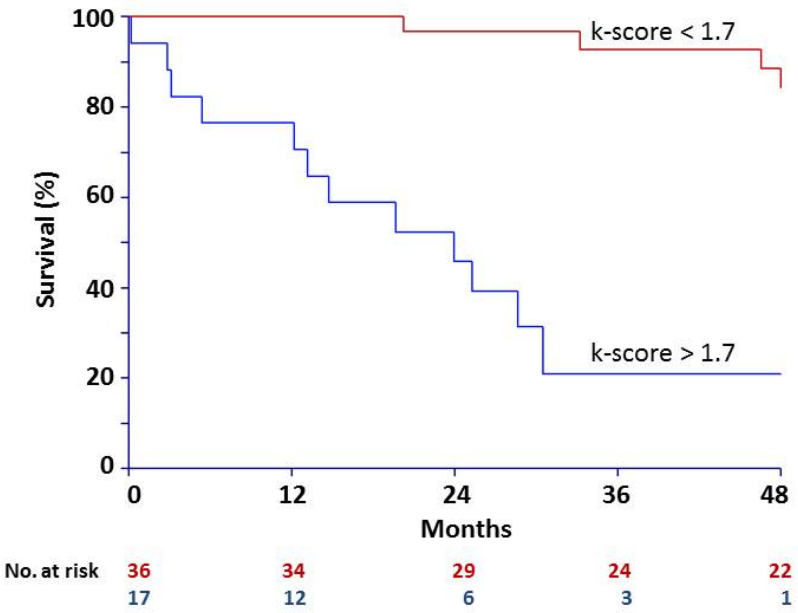

Figure 6: Kaplan-Meier survival curve based upon APV-ALT. APV-ALT prospectively predicted sustained VT/VF or implantable cardioverter-defibrillator therapy on Kaplan-Meier analysis (p=0.04). Solid line = APV-ALT; dashed line = sans APV-ALT.

References

[1] Jonathan D Moreno, Z. Iris Zhu, Pei-Chi Yang, John R Bankston, Mao-Tsuen Jeng, Chaoyi Kang, Lianguo Wang, Jason D Bayer, David J Christini, Natalia A Trayanova, Crystal M Ripplinger, Robert S Kass, and Colleen E Clancy. A computational model to predict the effects of class i anti-arrhythmic drugs on ventricular rhythms. *Sci Transl Med*, 3(98):98ra83, Aug 2011.

[2] P.A. Helm, R.L. Winslow, and E. McVeigh.

[3] Fijoy Vadakkumpadan, Hermenegild Arevalo, Anton J Prassl, Junjie Chen, Ferdinand Kickinger, Peter Kohl, Gernot Plank, and Natalia Trayanova. Image-based models of cardiac structure in health and disease. *Wiley Interdiscip Rev Syst Biol Med*, 2(4):489–506, 2010.

[4] Ferdinand Kickinger. www.meshing.at/spiderhome/tarantula.html.

[5] K. H W J ten Tusscher, D. Noble, P. J. Noble, and A. V. Panfilov. A model for human ventricular tissue. *Am J Physiol Heart Circ Physiol*, 286(4):H1573–H1589, Apr 2004.

[6] K. H W J ten Tusscher and A. V. Panfilov. Alternans and spiral breakup in a human ventricular tissue model. *Am J Physiol Heart Circ Physiol*, 291(3):H1088–H1100, Sep 2006.

[7] E. J. Vigmond, R. Weber dos Santos, A. J. Prassl, M. Deo, and G. Plank. Solvers for the cardiac bidomain equations. *Prog Biophys Mol Biol*, 96(1-3):3–18, 2008.

[8] Alexey V Glukhov, Vadim V Fedorov, Paul W Kalish, Vinod K Ravikumar, Qing Lou, Deborah Janks, Richard B Schuessler, Nader Moazami, and Igor R Efimov.

Conduction remodeling in human end-stage nonischemic left ventricular cardiomyopathy. *Circulation*, 125(15):1835–1847, Apr 2012.

[9] Qing Lou, Vadim V Fedorov, Alexey V Glukhov, Nader Moazami, Vladimir G Fast, and Igor R Efimov. Transmural heterogeneity and remodeling of ventricular excitation-contraction coupling in human heart failure. *Circulation*, 123(17):1881–1890, May 2011.

[10] Alexey V Glukhov, Vadim V Fedorov, Qing Lou, Vinod K Ravikumar, Paul W Kalish, Richard B Schuessler, Nader Moazami, and Igor R Efimov. Transmural dispersion of repolarization in failing and nonfailing human ventricle. *Circ Res*, 106(5):981–991, Mar 2010.

[11] Norbert Szentadrassy, Tamas Banyasz, Tamas Biro, Gergely Szabo, Balazs I Toth, Janos Magyar, Jozsef Lazar, Andras Varro, Laszlo Kovacs, and Peter P Nanasi. Apico-basal inhomogeneity in distribution of ion channels in canine and human ventricular myocardium. *Cardiovasc Res*, 65(4):851–860, Mar 2005.

[12] J. D. Bayer, R. C. Blake, G. Plank, and N. A. Trayanova. A novel rule-based algorithm for assigning myocardial fiber orientation to computational heart models. *Ann Biomed Eng*, 40(10):2243–2254, Oct 2012.

[13] David U J Keller, Daniel L Weiss, Olaf Dossel, and Gunnar Seemann. Influence of i(ks) heterogeneities on the genesis of the t-wave: a computational evaluation. *IEEE Trans Biomed Eng*, 59(2):311–322, Feb 2012.

[14] Shiho T Morita, Douglas P Zipes, Hiroshi Morita, and Jiashin Wu. Analysis of action potentials in the canine ventricular septum: no phenotypic expression of m cells. *Cardiovasc Res*, 74(1):96–103, Apr 2007.

[15] A. E. Pollard, M. J. Burgess, and K. W. Spitzer. Computer simulations of three-dimensional propagation in ventricular myocardium. effects of intramural fiber rotation and inhomogeneous conductivity on epicardial activation. *Circ Res*, 72(4):744–756, Apr 1993.

[16] B. J. Roth. Electrical conductivity values used with the bidomain model of cardiac tissue. *IEEE Trans Biomed Eng*, 44(4):326–328, Apr 1997.

[17] R. Studer, H. Reinecke, J. Bilger, T. Eschenhagen, M. Bhm, G. Hasenfuss, H. Just, J. Holtz, and H. Drexler. Gene expression of the cardiac na(+)-ca2+ exchanger in end-stage human heart failure. *Circ Res*, 75(3):443–453, Sep 1994.

[18] G. Hasenfuss, H. Reinecke, R. Studer, M. Meyer, B. Pieske, J. Holtz, C. Holubarsch, H. Posival, H. Just, and H. Drexler. Relation between myocardial function and expression of sarcoplasmic reticulum ca(2+)-atpase in failing and nonfailing human myocardium. *Circ Res*, 75(3):434–442, Sep 1994.

[19] R. H. Schwinger, M. Bhm, U. Schmidt, P. Karczewski, U. Bavendiek, M. Flesch, E. G. Krause, and E. Erdmann. Unchanged protein levels of serca ii and phospholamban but reduced ca2+ uptake and ca(2+)-atpase activity of cardiac sarcoplasmic reticulum from dilated cardiomyopathy patients compared with patients with nonfailing hearts. *Circulation*, 92(11):3220–3228, Dec 1995.

[20] M. Flesch, R. H. Schwinger, P. Schnabel, F. Schiffer, I. van Gelder, U. Bavendiek, M. Sdkamp, F. Kuhn-Regnier, and M. Bhm. Sarcoplasmic reticulum ca2+atpase and phospholamban mrna and protein levels in end-stage heart failure due to ischemic or dilated cardiomyopathy. *J Mol Med (Berl)*, 74(6):321–332, Jun 1996.

[21] H. Reinecke, R. Studer, R. Vetter, J. Holtz, and H. Drexler. Cardiac na+/ca2+ exchange activity in patients with end-stage heart failure. *Cardiovasc Res*, 31(1):48–54, Jan 1996.

[22] S. O. Marx, S. Reiken, Y. Hisamatsu, T. Jayaraman, D. Burkhoff, N. Rosemblit, and A. R. Marks. Pka phosphorylation dissociates fkbp12.6 from the calcium release channel (ryanodine receptor): defective regulation in failing hearts. *Cell*, 101(4):365–376, May 2000.

[23] Donald M Bers, David A Eisner, and Hector H Valdivia. Sarcoplasmic reticulum ca2+ and heart failure: roles of diastolic leak and ca2+ transport. *Circ Res*, 93(6):487–490, Sep 2003.

[24] Lai-Hua Xie, Daisuke Sato, Alan Garfinkel, Zhilin Qu, and James N Weiss. Intracellular ca alternans: coordinated regulation by sarcoplasmic reticulum release, uptake, and leak. *Biophys J*, 95(6):3100–3110, Sep 2008.

[25] Thomas R Shannon, Steven M Pogwizd, and Donald M Bers. Elevated sarcoplasmic reticulum ca2+ leak in intact ventricular myocytes from rabbits in heart failure. *Circ Res*, 93(7):592–594, Oct 2003.

[26] Thomas R Shannon, Fei Wang, and Donald M Bers. Regulation of cardiac sarcoplasmic reticulum ca release by luminal [ca] and altered gating assessed with a mathematical model. *Biophys J*, 89(6):4096–4110, Dec 2005.

[27] Y. Pron, S. Demolombe, I. Bar, E. Drouin, F. Charpentier, and D. Escande. Differential expression of kvlqt1 isoforms across the human ventricular wall. *Am J Physiol Heart Circ Physiol*, 278(6):H1908–H1915, Jun 2000.

[28] D. J. Beuckelmann, M. Nbauer, and E. Erdmann. Alterations of k+ currents in isolated human ventricular myocytes from patients with terminal heart failure. *Circ Res*, 73(2):379–385, Aug 1993.

[29] Gui-Rong Li, Chu-Pak Lau, Tack-Ki Leung, and Stanley Nattel. Ionic current abnormalities associated with prolonged action potentials in cardiomyocytes from diseased human right ventricles. *Heart Rhythm*, 1(4):460–468, Oct 2004.

[30] M. Nbauer, D. J. Beuckelmann, P. Uberfuhr, and G. Steinbeck. Regional differences in current density and rate-dependent properties of the transient outward current in subepicardial and subendocardial myocytes of human left ventricle. *Circulation*, 93(1):168–177, Jan 1996.

[31] Carmen R Valdivia, William W Chu, Jielin Pu, Jason D Foell, Robert A Haworth, Mathew R Wolff, Timothy J Kamp, and Jonathan C Makielski. Increased late sodium current in myocytes from a canine heart failure model and from failing human heart. *J Mol Cell Cardiol*, 38(3):475–483, Mar 2005.

[32] Thomas O'Hara, Lszl Virg, Andrs Varr, and Yoram Rudy. Simulation of the undiseased human cardiac ventricular action potential: model formulation and experimental validation. *PLoS Comput Biol*, 7(5):e1002061, May 2011.

[33] Jun-Ichi Okada, Takumi Washio, Akiko Maehara, Shin-Ichi Momomura, Seiryo Sugiura, and Toshiaki Hisada. Transmural and apicobasal gradients in repolarization contribute to t-wave genesis in human surface ecg. *Am J Physiol Heart Circ Physiol*, 301(1):H200–H208, Jul 2011.

[34] Michiel J Janse, Ruben Coronel, Tobias Opthof, Eugene A Sosunov, Evgeny P Anyukhovsky, and Michael R Rosen. Repolarization gradients in the intact heart: transmural or apico-basal? *Prog Biophys Mol Biol*, 109(1-2):6–15, May 2012.

[35] Sanjiv M Narayan, Jason D Bayer, Gautam Lalani, and Natalia A Trayanova. Action potential dynamics explain arrhythmic vulnerability in human heart failure: a clinical and modeling study implicating abnormal calcium handling. *J Am Coll Cardiol*, 52(22):1782–1792, Nov 2008.

[36] E. J. Vigmond and L. J. Leon. Electrophysiological basis of mono-phasic action potential recordings. *Med Biol Eng Comput*, 37(3):359–365, May 1999.

[37] Kazutaka Gima and Yoram Rudy. Ionic current basis of electrocardiographic waveforms: a model study. *Circ Res*, 90(8):889–896, May 2002.

[38] Sanjiv M. Narayan, Michael R. Franz, Paul Clopton, Etienne J. Pruvot, and David E. Krummen. Repolarization alternans reveals vulnerability to human atrial fibrillation. *Circulation*, 123(25):2922–2930, Jun 2011.

[39] A. L. Ritzenberg, D. R. Adam, and R. J. Cohen. Period multupling-evidence for nonlinear behaviour of the canine heart. *Nature*, 307(5947):159–161, 1984.

[40] Bruce D. Nearing and Richard L. Verrier. Progressive increases in complexity of t-wave oscillations herald ischemia-induced ventricular fibrillation. *Circ Res*, 91(8):727–732, Oct 2002.